It's just a phase: high-contrast imaging with patterned liquid-crystal phase plates to facilitate characterization of exoplanets

Doelman, D.S.

8 Multi-color holography with a two-stage patterned liquid-crystal element

Adapted from
D. S. Doelman, M. J. Escuti, F. Snik
Published in Optical Materials Express (2019)

Computer-generated Geometric Phase Holograms (GPHs) can be manufactured with high efficiency and high fidelity using photo-aligned liquid crystals. GPHs are diffractive elements, which therefore have a wavelength-dependent output and can generally not be used for the production of color imagery. We implement a two-stage approach that first uses the wavelength-dependent diffraction to separate colors, and second, directs these colors through separate holographic patterns. Moreover, by utilizing the geometric phase, we obtain diffraction efficiencies close to 100% for all wavelengths. We successfully create a white light hologram from RGB input in the lab. We demonstrate that this schematic allows for full control over individual (RGB) channels and can be used for wide-gamut holography by selecting any combination of wavelengths. In addition, we show with simulations how this two-stage element could be used for of true-color holograms with applications in high contrast imaging.

8.1 Introduction

Computer generated holography is the art of shaping light into custom 2D and 3D intensity profiles, often used to recreate the image of an object or a scene (Brown & Lohmann, 1966, 1969; Slinger et al., 2005; Lohmann, 2008; Yaraş et al., 2010). An optical element that encodes a computer generated hologram (CGH) must be able to change the phase or amplitude of light and must be programmable at least once for passive holography or multiple times for adaptive holography. In general, liquid-crystal (LC) layers are able to change phase, polarization and amplitude of light, depending on the orientation of the optic axis and surrounding films. A specific type of phase element that can be manufactured with LCs is a geometric-phase hologram (GPH) (Escuti et al., 2016; Kim et al., 2015; Hasman et al., 2003; De Sio et al., 2016). GPHs generate geometric phase shifts, wherein a phase change arises from the geometry of the evolution the light through the anisotropic medium. When LCs are used to form GPHs, this anisotropy occurs due to the material's birefringence, and this is also sometimes called the Pancharatnam-Berry phase (Pancharatnam, 1955; Berry, 1984; Anandan, 1992).

Besides liquid crystals, there are other materials capable of generating geometric phase holograms. These materials are made of metasurfaces or nano-structures and allow for full control of phase, amplitude and polarization simultaneously (Huang et al., 2013; Ni et al., 2013; Mueller et al., 2017). However, these materials still suffer from high scattering or low efficiencies, especially for broadband light ($\Delta\lambda/\lambda > 30\%$) (**?**Huang et al., 2016). Therefore we focus on liquid-crystal GPHs.

A LC GPH operates on circular polarization, *i.e.,* an incoming lightwave is decomposed into the two circular polarization states and the sign of the geometric phase depends on the handedness of each state. Its wavefront may be spatially varied by locally varying the orientation, Φ, of in-plane optic axis of the LC. The resulting geometric phase, δ, depends on the orientation and the handedness of the circular polarization according to

$$\delta(x, y) = \pm 2\Phi(x, y). \tag{8.1}$$

Creating arbitrary patterns is possible with a photo-alignment layer (PAL) (Chigrinov et al., 2008). Polymers in the PAL record the orientation of incoming linearly-polarized UV radiation and direct-write laser scanning (Miskiewicz & Escuti, 2014; Kim et al., 2015) allows for writing arbitrary patterns with high precision. The initial orientation pattern in the PAL and first LC layer is passed on to subsequent layers by spontaneous self-alignment. In this way, LC layers with different thickness and chiral twists may be arranged into a monolithic film (Komanduri et al., 2013). The many degrees of freedom of these multi-twist retarder (MTR) films may be used to tune the retardation of the LC layer to half-wave retardance, achieving high efficiency (Kim et al., 2015; Escuti et al., 2016) in GPHs over large bandwidths into a single diffracted order. Furthermore, GPHs are ideal to record CGHs as they can be manufactured with unbounded continuous phase, wide angular bandwidths, and very high spatial frequencies (Xiang et al., 2017a, 2018, 2017b).

The simplest example of a GPH is a polarization grating (PG). A PG has a linear ramp in phase in one direction, similar to a refractive prism. The two circular-polarization states are diffracted in opposite directions and the leakage is directly transmitted, corresponding to the first- and zero-diffraction orders, respectively. The broadband diffraction efficiencies for PGs can be manufactured to be close to 100% for the full visible range (Oh & Escuti, 2008). Similar to any other grating, the diffraction angle of a PG is dependent on wavelength. This is common for all GPHs. A computer generated Fraunhofer CGH will therefore have the same intensity distribution for all wavelengths, only wavelength-scaled (Xiang et al., 2017a). Note that CGHs created with dynamic phase elements, *i.e.,* produced by locally changing the optical path length, have decreased fidelity for wavelengths than other than the one the pattern was optimized for. For Fresnel CGHs the size of the hologram is the same for each wavelength, but the imaging position is now wavelength-dependent (Jesacher et al., 2014; Huang et al., 2016).

Generating multi-color holograms requires encoding different phase patterns for individual colors. Not only is the intensity distribution of the hologram usually different for each color, even generating the same intensity distribution for each color also requires scaling the phase to match the wavelength. For clarity, we enumerate here the different methods that generate multi-color holograms by the number of used elements. A first method uses volume holograms that stores the color information in a single thick optical element (Leith et al., 1966). A second set of methods use spatial light modulator (SLM). One uses shutters to illuminate the SLM with only one color at the time (Shimobaba & Ito, 2003). Fast switching of the color and phase pattern generates the illusion of a color hologram. In another, the SLM is combined with color filters for pixel columns, such that the RGB channels each acquire the desired phase (Tsuchiyama & Matsushima, 2017). Finally, it is also possible to use an SLM with a large dynamic range $(0 - 10\pi)$ to encode a single multi-color hologram (Jesacher et al., 2014). A third method optimizes the phase pattern of a SLM to generate the RGB holograms spatially separated in the propagation direction (Makowski et al., 2008). Each color generates three consecutive holograms calculated for a specific distance using Fresnel propagation. At one specific distance all three colors combine to a single multi-color hologram. Similarly, it is also possible to separate the input spatially in the same image plane (Ito & Okano, 2004). When the RGB inputs originate from a different point on the image plane, all elements could have the same phase and combine in the center to a multi-color hologram.

Multi-element systems for color holography usually separate the light. Analogous to standard projection systems, most multi-element holography systems separate white light in RGB arms, each with its own SLM, using dichroic mirrors and beamsplitter cubes and recombining them in a similar fashion (Shiraki et al., 2009). This complex optical system uses three phase elements (SLMs) for the RGB channels.

In this paper we propose a simpler two-stage system capable of producing multi-color holograms with high efficiency.

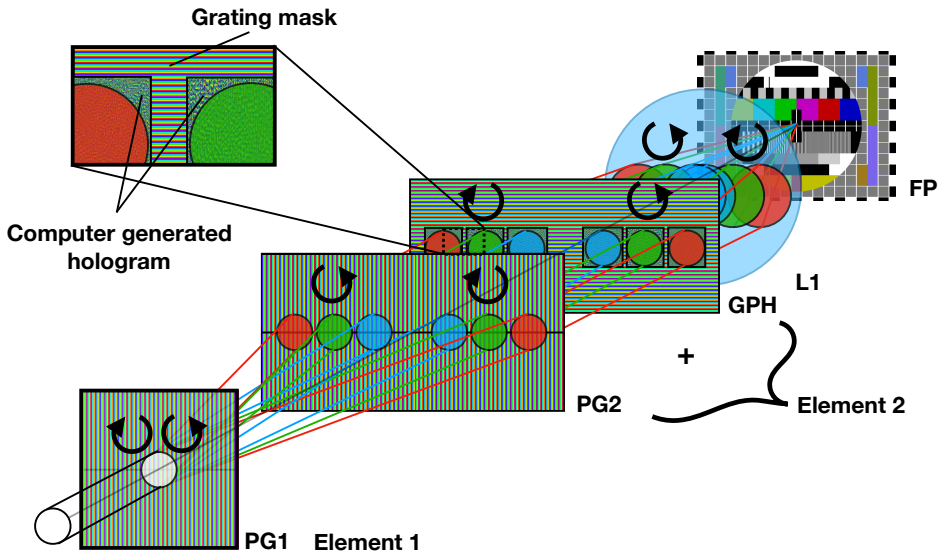

Figure 8.1: Schematic of the multi-color geometric phase hologram. A polarization grating (PG1) separates the multi-color input. A second stage collimates the beams with a polarization grating (PG2) and add the individual computer generated geometric phase hologram (GPH) to the pupils with different colors. A lens combines both circular polarizations to form one multi-color hologram. The second stage can be composed of two separate elements or comined into one single element.

8.2 Concept of multi-color liquid-crystal holography

As discussed above, GPHs are efficient over a large bandwidth and apply wavelength-independent geometric phase shifts (Xiang et al., 2017a). However, they have so far not been used much for multi-color holography as they are diffractive, generating wavelength scaled holograms. We present a two-stage element that produces a multi-color hologram by separating different colors with a PG and applying individually tuned CGHs, embodied as GPHs, to each color. The concept is shown in Fig. 8.1. A white-light pupil, containing equal amounts of red, blue and green light, is diffracted by the polarization grating. A polarization grating (PG) separates the pupil with efficiencies close to 100% in the ± 1-orders, where the intensity distribution between the $+1$ and -1 order depends on the amount of circular polarization in the source. The second stage does two things simultaneously. First, it collimates the light with a polarization grating pattern that is exactly the same as the first element. The beam is collimated with high efficiency because the polarization gratings have polarization memory. In addition, the second stage adds

the phase delay corresponding to the CGH for each individual color. Because the colors are separated, the CGH can be adjusted to make the correct intensity distribution for each wavelength. Combining the computer generated hologram with the polarization grating is possible because a polarization grating effectively adds a geometric phase tilt to the beam and can therefore be added in phase to the CGH pattern (Doelman et al., 2017). Finally, a high-frequency grating pattern can be added outside of the CGH to diffract light outside of the pupil away from the hologram. This grating mask (Doelman et al., 2017), removes the need for individual amplitude masks for individual colors. For clarity, the two phase patterns (PG and GPH) are shown in a consecutive order in Fig. 8.1. When the phase delays are applied to the collimated beams, all colors can be recombined in the image plane by imaging the beam with a lens. It is also possible to propagate to the far field, however the different colors will not overlap.

For the best result, individual colors need to be separated by the multi-color geometric phase hologram. This means that the distance between the two elements, d, and the grating frequency, n, need to be tuned to the hologram properties. Here n is the number of periods per meter. To make sure two pupils of different color do not overlap, the distance between the centers of the phase patterns, ΔL, is given by

$$\Delta L = d(\tan(n\lambda_2) - \tan(n\lambda_1)) > D, \tag{8.2}$$

Where D is the physical size of the computer generated holographic phase pattern and λ_1 and λ_2 are the two selected wavelengths where $\lambda_2 > \lambda_1$. When pupils overlap, two colors start mixing and this generates a scaled hologram similar to classical geometric phase holograms. The distance between the two elements is a free parameter and can be used to accommodate the correct separation.

Because the colors are physically separated, there is no requirement on the hologram shape or phase from other wavelengths. Therefore, the phase patterns that generate the hologram can be calculated individually. Individual color channels can have different shapes or sizes as long as it produces the desired holographic intensity distribution. For example, when generating a white-light hologram (the RGB channels produce the same hologram), the phase pattern can be scaled to match the wavelength dependent diffraction limit. To generate the phase patterns we use the Gerchberg-Saxton (GS) algorithm (Gerchberg & Saxton, 1972) implemented in HCIPy (Por et al., 2018). GS iterates between the focal and pupil plane and applies the pupil shape and the desired focal plane intensity as constraint, keeping the calculated phase. This way, arbitrary intensity distributions can be calculated.

Because the multi-color GPH combines liquid-crystal elements with high efficiencies and polarization memory, the multi-color GPH achieves close to 100% efficiency when using both circular polarization states. For larger holograms where the distance between left- and right-circular polarization becomes significant, imaging both with the same lens becomes impractical. Selecting one polarization reduces the efficiency by a factor of 2, but allows for a more compact system. Both circular-polarization states can also be used to create different holograms for re-

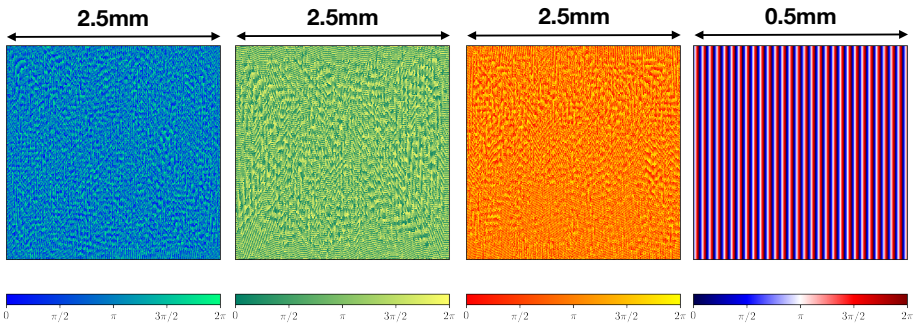

Figure 8.2: The phase designs for the computer generated holograms tested in the lab. The left panel shows the phase design for the blue laser ($450nm$), as indicated by the colormap. Similarly, the two center panels show the green and red phase design. The right panel shows the zoomed pattern corresponding to the polarization grating.

ducing speckles in the image with more homogeneous illumination and accessing different spatial frequencies (Kowalczyk et al., 2018). Taking this further, the two circular polarization states can create individual holograms for stereoscopic 3D holography. This is fully compatible with circularly polarizing eyewear for viewing projected stereoscopic motion pictures.

8.3 Lab experiment and result

8.3.1 Design of the multi-color geometric phase holograms

Next we test the concept of the multi-color geometric phase patterns. Using the Gerchberg-Saxton algorithm we generate three phase patterns for a focal plane hologram containing two separate neighbouring structures. The first structure is only wavelength scaled such that all three colors add to one white light hologram. The second structure was generated to test color blending necessary for wide gamut holography. We vary the intensity distribution in one direction only, adapted to combine the three colors at different intensity values. We place the three holograms next to each other as the ratio between the red (440 nm), green (510 nm), and blue (635 nm) is approximately the same. The three holograms can be operated in stand-alone mode, *i.e.* they do not contain the polarization grating. Figure 8.2 shows the fabricated phase patterns calculated for a square aperture. For clarity, the panels have different color maps that match the three colors belonging to the wavelengths the holograms are calculated for. A segment of the PG pattern is also shown in Fig. 8.2, the total size of both PGs is $10mm$, the three holograms have 5μm pixels, totalling 500 pixels. The period of the two polarization gratings is set to 17 μm to generate a more compact setup. The grating pattern was calculated

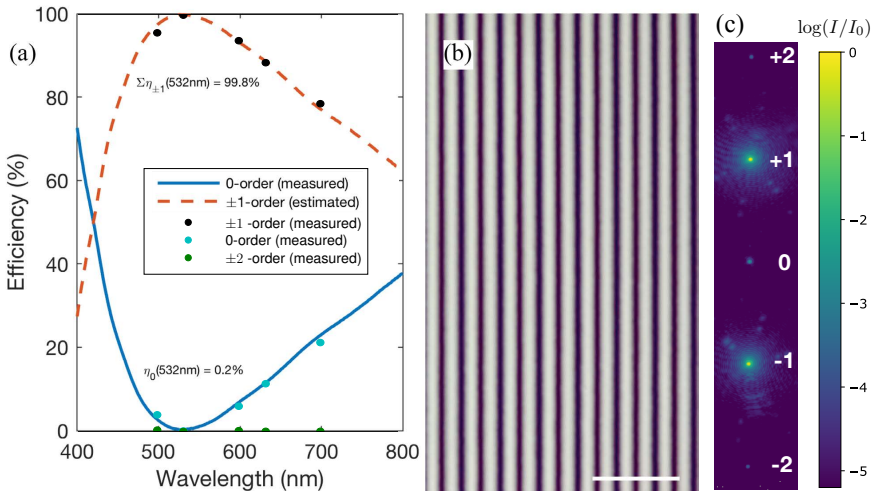

Figure 8.3: Measured properties of the fabricated PG: (a) diffraction efficiencies of the zero-, total first- and second-orders; (b) polarizing optical micrograph, where the scale bar indicates 50 μm; and (c) the PSF of the PG at 532nm that includes the first two diffraction orders, showing that the second-order diffraction efficiency is $<<$ 1%.

with a pixel size of 1μm. The patterns are checked for high gradients between single pixels to prevent disclination lines from appearing. No changes were made to the phase pattern as the gradients are mostly well behaved.

8.3.2 Manufacturing process

Fabrication begins with coating the azo-based photo-alignment layer (Chigrinov et al., 2008) LIA-CO01 (DIC Corp) on clean glass (D263) substrates (spin: 30 s @ 1500 rpm, bake: 60 s @ 130°C), about 30 nm thick. For exposure, we employ the direct-write laser scanning system described in Refs. (Miskiewicz & Escuti, 2014; Kim et al., 2015), using a solid-state 355 nm laser (Coherent Inc) delivering an exposure energy of about 1 J/cm^2. The PG pattern was simply a linear phase profile, while the three hologram phase patterns were discussed in the prior section, all sampled with 5 μm resolution. Both plates were processed and scanned in the same way, except for the scanned orientation profile. For the first liquid crystal polymer (LCP) network sublayer, we use a solution comprising solids RMM-A (Merck KGaA, $\Delta n = 0.16$ @ 532 nm) in solvent propylene-glycol-methyl-ether-acetate (PGMEA from Sigma-Aldrich), with a 5% solids concentration. This was processed (spin: 55 s @ 1200 rpm, cure: 30 s @ 190 mW of UV illumination from a 365 nm LED in dry nitrogen environment). For the second and third sublayers, we use a second solution, comprising 20% RMM-B (Merck KGaA, $\Delta n = 0.25$ @ 532 nm) in solvent PGMEA. This is processed (spin and cure steps identical to

the first LCP sublayer except for spin at 700 rpm). This lead to a total thickness of approximately 1.1 μm, as measured by an ellipsometer, which is a half-wave retardation around 532 nm.

In Fig. 8.3, we show measured properties of the fabricated PG. We were not able to directly measure the holograms in the same way due to their much more complex phase pattern. All samples had no observable haze and nearly all the output power appeared in the zero- and first-orders. Fig. 8.3(a) shows the measured zero-order efficiency spectrum of the PG, where $\eta_0 = 0.2\%$ at 532 nm and was below 50% for the red and blue wavelengths. The total first-order efficiency was estimated as $\Sigma\eta_{\pm 1} = 100\% - \eta_0$, also shown. We can therefore estimate $\Sigma\eta_{\pm 1} = 99.8\%$ at 532 nm. Both of these efficiency measurement should also apply to the three holograms, because the LCP coating was the same. A polarizing optical microscope was used to capture the LC texture of the PG, showing a smoothly varying sinusoidal variation in intensity, which indicates a very linear phase (*i.e.*, LC optic axis orientation).

8.3.3 Lab setup

We test the liquid-crystal geometric phase holograms in the lab using three laser diode modules as input. The laser diodes are the CPS450, CPS532a and CPS635S from Thorlabs, operating at 450 nm, 532 nm, and 645 nm respectively. We use the equal power of the lasers to match the input color intensity with the RGB response of the camera. We combine the beams in a single mode fiber using two 50/50 beamsplitters and a lens. The single mode fiber (SMF) creates a diffraction limited beam as input for the multi-color GPH. The light from the SMF is collimated and stopped down to the size of 2 mm. The first polarization grating diffracts the light off-axis. We use a second aperture to filter out the leakage light and the opposite circular polarization state. The second PG collimates the light and the GPH applies the phase of the computer generated hologram. A circular polarizer is used to filter out the GPH leakage term and the three pupils are imaged on a Canon EOS 6D CMOS camera. The setup is shown in Fig. 8.4.

Both structures in the hologram are imaged simultaneously with the camera. The Canon EOS 6D CMOS is a color camera, the color space is set to sRGB and we extract the raw frames directly.

8.3.4 Experimental results

We image the holographic structures with the three different colors and all combinations. The results are displayed in Fig. 8.5. The first structure, the polygon, has all three colors overlapping in both dimensions. Each combination of the colors, shown in the second row, produces the expected colors, being yellow, cyan and magenta from left to right. The colors are slightly saturated. However, the RGB combination in the bottom row clearly shows a white light hologram, with matching scales for the individual colors. This demonstrates that each pupil acquired the phase from the pattern designed for that wavelength and that the pupils do

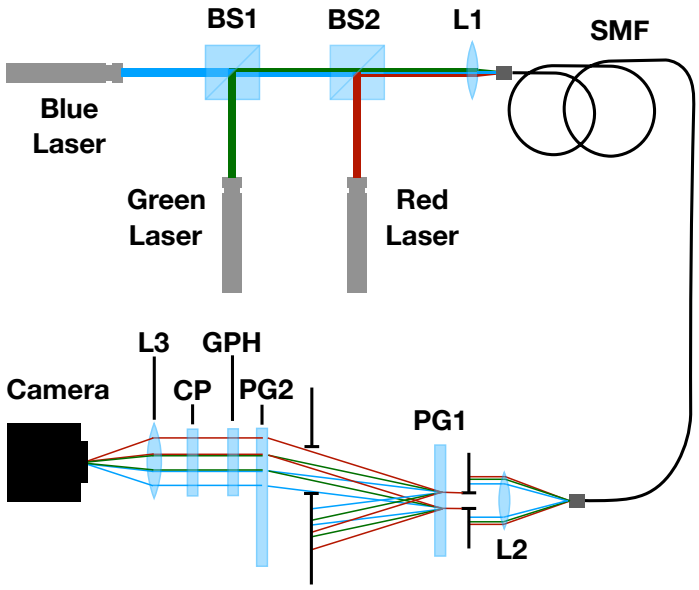

Figure 8.4: Lab setup used to test the multi-color GPH. The three lasers are combined with two beam splitters (BS) and imaged with a lens (L1) on a single mode fiber (SMF). The light from the SMF is collimated with a second lens (L2). Two irises create the pupil and select a single circular polarization from the two polarization gratings (PGs). A circular polarizer (CP) is used to filter leakage and third lens (L3) images the hologram on the detector.

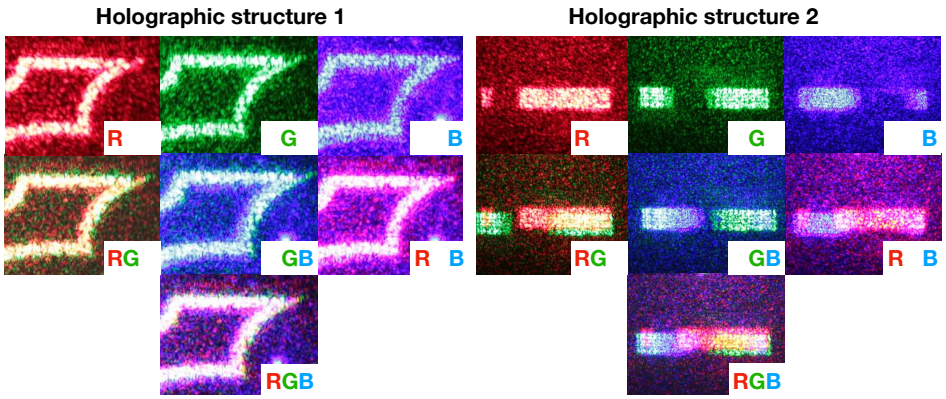

Figure 8.5: Measured intensity of the holograms for each combination of the RGB input colors. The multi-panel image on the left shows the first structure of the hologram, a 2D polygon. On the right is the one dimensional second structure with varying intensities, producing multiple colors.

not overlap. The second structure contains intensity variations in the x-direction and this allows to access different colors in the color space than the first structure. Both structures show that the multi-color GPH is capable of producing a multi-color hologram.

We selected the three laser diodes because of their equal power of 4.5 mW. The green laser has some offset compared to the designed wavelength, 532 nm instead of 510 nm. This can be seen both structures of the hologram, the green one is slightly larger and offset compared to the red and blue images. Moreover, both structures contain speckles instead of a more homogeneous intensity distribution. This is a well known problem for the Gerchberg-Saxton (GS) algorithm (Kuratomi et al., 2010; Pan & Shih, 2014) and can be solved by implementing the double-constraint Gerchberg-Saxton algorithm (Chang et al., 2015). In addition, there is a non-zero background with speckles that is not part of the structures. This background should not be attributed to the scattering of the liquid-crystal film (Xiang et al., 2017a), but rather, to the hologram phase design. In this design the hologram has a background that is only suppressed by a factor of 100, and can still be seen by the camera.

8.4 Wide-gamut and true-color holography

8.4.1 Color selection

Multi-color geometric phase holograms are not limited to RGB holography. The polarization grating physically separates all colors in a spectrum and the GPH can modify them individually when the differently colored pupils are separated.

Selecting more or other colors than RGB can create a more natural hologram, *i.e.*, the spectrum is closer to the reflectance spectrum of the object the hologram represents (Peercy & Hesselink, 1994). Note that the difference in color rendition of most objects with more than seven different wavelengths is almost indistinguishable for the human eye (Bjelkhagen & Mirlis, 2008). The optimal wavelength selection for 3-5 different colors is written in Bazargan et al. (Bazargan, 1992). Any number of separate holograms can be added as long as the separation follows Eq. 8.2 and the combined width is still within the manufacturing range ($<$ 30 cm (Kim et al., 2015)). Using more colors with a constant pupil size requires an increase in d, the distance between the elements, or an increase in the grating frequency n. The latter is limited by the writing resolution of the direct-write system, the former is limited by available space.

8.4.2 True-color holography

The multi-color geometric phase hologram also works with a white light source. With the white light source, the second element is illuminated with a continuum of dispersed pupils. This requires a different method of optimization of the phase pattern, where the phase pattern is calculated for all wavelengths simultaneously. However, using a white-light source gives access to the full gamut space and allows for generating the actual reflectance spectrum for even the most exotic objects.

To evaluate this concept, we investigate true-color geometric phase holograms in simulation. We divide the phase pattern with a width of 4 pupil diameters in 36 different colors, or wavelength bins, with overlapping pupils. Each color has its own focal plane constraint, *i.e.*, the desired intensity in the focal plane is a function of wavelength. The focal plane design is shown in the top right of Fig. 8.6. Note that the locations where the RGB colors normally overlap have been purposefully replaced by the wrong colors. They are not formed by the combination of RGB light but the light that is directed in these regions has a wavelength corresponding to the indicated color, *i.e.*, a true-color hologram. In addition, this hologram design is specifically good for checking color blending from overlapping pupils. Therefore, we replace magenta by violet, as magenta, being a combination of blue and red colors, is already blended. The constraints as function of wavelength are shown with dotted lines in bottom left of the same figure. We start with a uniform pupil and a random phase for each color and perform one iteration of GS. After applying the pupil plane mask for each wavelength, we mean-combine all phases to a single phase pattern, masking the regions that do not overlap and would add zeros to the mean. Because the pupil plane sampling is high and the focal plane constraint is smooth in wavelength, the individual phase patterns are similar for neighbouring colors. Therefore, averaging does not remove the calculated phase entirely and the algorithm converges when the averaged phase is used as input for the next iteration.

The combined phase pattern is shown on the top left of Fig. 8.6 and has 500x100 pixels. The color of the light the phase pattern is illuminated with is indicated by the color bar on top of the phase pattern. The phase pattern shows roughly six

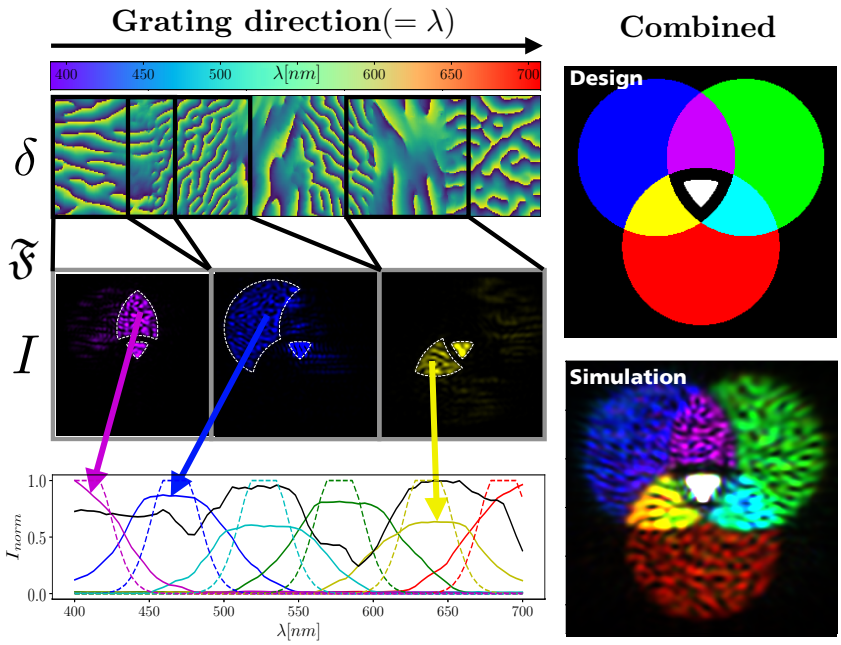

Figure 8.6: Simulation of a true-color hologram with a two-stage geometric phase hologram (GPH). A square pupil is dispersed by the first grating over a width of four pupil diameters when arriving at the GPH. *Top left:* the central color of the pupils is indicated by the color bar and the phase pattern is shown below. *Top right:* the design of the hologram, were the intersection of the RGB circles are purposely altered. *Center left:* Three pupils are selected and with Fourier propagation the intensities are calculated. *Bottom right:* The summed intensities multiplied in the six regions indicated for the six different colors as function of wavelength (solid line). The normalized spectrum of the center (white light) is shown in black. The images show reasonable agreement with the input spectra (dotted line). *Bottom right:* the combined hologram, integrated over all colors, converted to RGB. The simulation shows that using a two-stage GPH is capable of producing true-color holograms.

different regimes in the grating direction, corresponding to the six colors in the designed hologram. The bottom left in Fig. 8.6 show the hologram for a single wavelength and in solid lines the summed and normalized intensity in the differently colored regions. It is clear that the spectra of the colors are not perfectly constrained, the drop-off is much slower than designed and the intensities are not equal but deviate by a factor 2. The drop-off is mostly constrained by the pupil overlap, *i.e.*, the ratio of the phase plate width and the pupil diameter, and the gradient in the desired holographic spectrum. For this simulated full-color hologram the dominating colors in the overlapping regions are still the same as in the design. We calculate the colors by summing the focal plane intensities as function of wavelength multiplied by the design spectrum. This gives the holographic intensities for six colors. We calculate the RGB colors by spitting the cyan, violet and yellow colors evenly over the RGB channels. We normalize the intensities on the central white light region and saturate it to make the colors more visible. Overall the simulated hologram is in good agreement with the design, showing that in simulation true-color holography is possible with a two-stage liquid-crystal element.

The advantage of this two-stage liquid-crystal element for holography are the high efficiency and high-fidelity simultaneous beam shaping for multiple wavelengths and opposite circular polarization states. In the presented state with passive liquid-crystal films it is only possible to generate static holograms. Therefore, this technology is easily applicable for projection, either on a reflective surface or directly into the eye of an observer. In addition, when using the two opposite circular polarization states it is possible to make 3D stereoscopic holograms. These properties make the two-stage system interesting for the field of visual arts.
Making an active two-stage element is possible by replacing the geometric phase hologram with a separate polarization grating and a spatial light modulator (SLM). When the wavelengths are separated by two polarization gratings, the phase errors from using classical phase are relatively small. Such an active two-element system has a wider range of applications. Most notably, scientific applications like optical tweezers, where multi-wavelength intensity field manipulation could be useful for optical manipulation of microparticles with different absorption spectra (Hayasaki et al., 1999; Grier, 2012). Compared to the phase contrast image synthesis method (Glückstad, 1996; Palima & Glückstad, 2008), the two-stage element allows for different beam shapes for multiple wavelengths, giving more freedom for particle manipulation.

8.4.3 True-color vAPP coronagraphs

Another possible implementation of the true-color holograms is in the field of direct imaging of extra-solar planets (exoplanets). The light of exoplanets is 10^4- 10^{10} times fainter than the stellar light, and exoplanets orbit close to the star compared to the distance relative to Earth. The angular separation is often less than an arcsecond, 1/3600th of a degree, which is only a few diffraction widths away for the largest telescopes. The diffraction structure of a stellar PSF is many

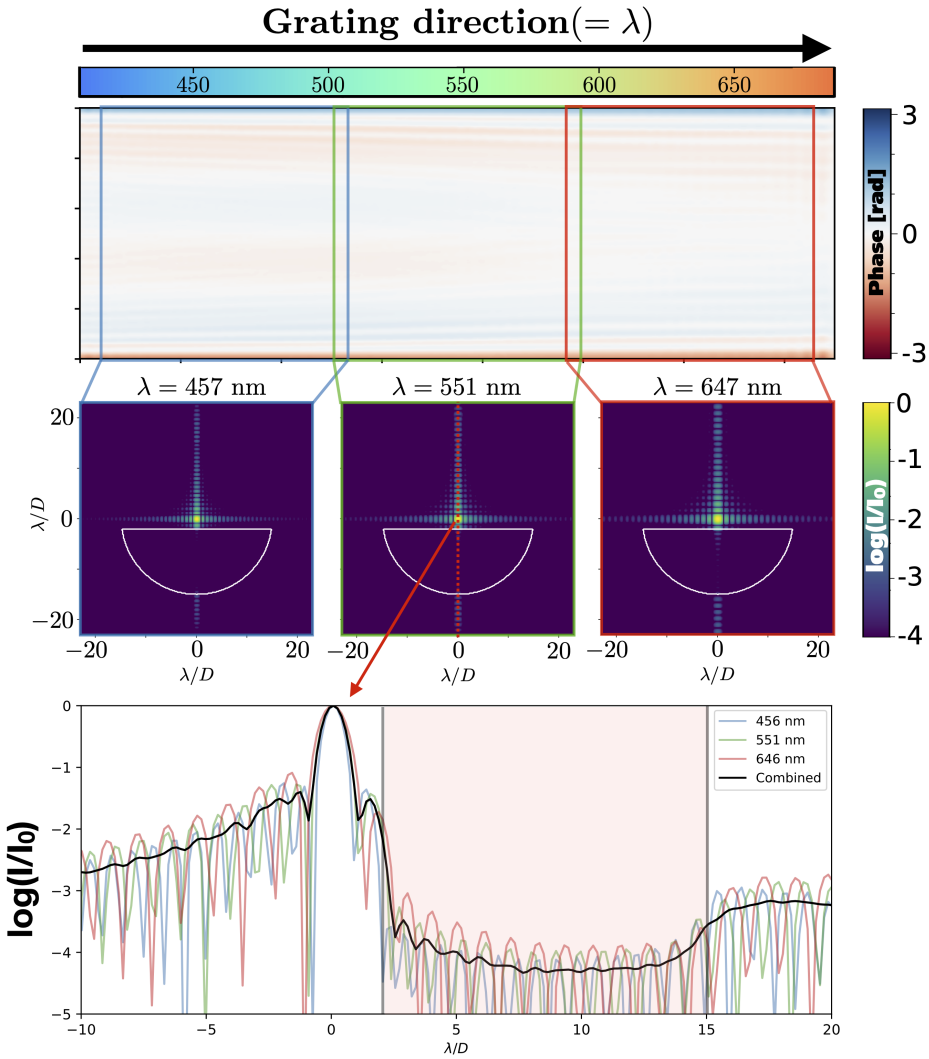

Figure 8.7: Simulation of a true-color vAPP hologram with a two-stage geometric phase hologram (GPH). The vAPP design is calculated using the same algorithm as the design presented in Fig. 8.6. The dark zone extends from 2-15 λ/D.

orders of magnitude brighter than the signal of the exoplanets. Optical components that remove the diffraction structure of on-axis sources are called coronagraphs, named after the first use of a such a device by Bernard Lyot to observe the solar corona (Lyot, 1939). A specific type of coronagraph is a phase only optic that is installed in the pupil plane called the grating vector-Apodizing Phase Plate (gvAPP) coronagraph (Snik et al., 2012; Otten et al., 2017), which is explained in more detail in chapter 2. The gvAPP creates two PSFs with a region called the dark zone, where the diffraction structure is nulled and exoplanets can be detected (Otten et al., 2014). These two PSFs are created by separating the two circular polarization states with the grating and have dark zones on opposite side, as follows from Eq. 8.1. The gvAPP coronagraph is also manufactured using the liquid-crystal technology described in this chapter. The gvAPP coronagraphs are installed in many different direct imaging instruments and have two properties that are suboptimal for exoplanet imaging. Their grating is necessary to separate the two circular polarization states from each other and the leakage term, yet the dispersion smears planet light over many pixels, introducing more noise. Secondly, the separation of circular polarization states directs half of the light in the bright-side of vAPP PSF, reducing the throughput of the planet light by a factor of 2. These two problems can be solved with a two-stage vAPP GPH.
The first grating of the GPH is unchanged and physically separates the two circular polarization states and the leakage term, just like the grating of the gvAPP. With the second stage, the phase pattern can be designed to generate two coronagraphic PSFs that have the dark zone on the same. Also, the phase pattern can be changed as function of wavelength to have the dark zone at the same physical distance from the PSF core. This increases the throughput of the star and exoplanet for the shortest wavelengths. Lastly, the polarization leakage can be blocked by a two-stage vAPP GPH coronagraph as it is physically separated from the main beams. We generated a true-color vAPP phase pattern using the GS algorithm, which is shown in Fig. 8.7. The dark zone extends from 2-15 λ/D, and has an average stellar suppression ratio of $> 10^4$ in this region. The slices of the PSF intensity through the strongest diffraction structure from a square pupil are also shown for three colors. These slices show how the diffraction structure is different as function of wavelength. Important is that the inner edge of the dark zone still shifts with wavelength, which is most likely caused by the constraint that the phase pattern must be smooth. A square pupil is also not ideal for telescopes with circular apertures, reducing the area by a factor $2/\pi \sim 0.64$. Optimizing the phase pattern for a more realistic telescope aperture is left as a future exercise.

8.5 Conclusion

We propose and demonstrate a two-stage patterned liquid-crystal element for multi-color holography. We separate colors by using the diffractive properties of a polarization grating (PG). A second element collimates the light and applies a computer generated geometric phase hologram, calculated for the separated colors individually. We show that the polarization memory of the PGs allows for efficiencies close to 100% for all visible wavelengths. In addition, we demonstrate full control over the individual colors and show that this concept can be adapted beyond RGB only to allow for wide-gamut holography. We validate with lab measurements that the multi-color liquid-crystal element produces color holograms unaffected by wavelength scaling. Lastly, we present a modified Gerchberg-Saxton algorithm for calculating white-light geometric phase holograms with dispersed pupils as input and apply it to design an improved vAPP coronagraph.

Acknowledgements

We thank Shuojia Shi for assistance in fabrication and Merck KGaA for customized materials.

Funding

The research of David S. Doelman and Frans Snik leading to these results has received funding from the European Research Council under ERC Starting Grant agreement 678194 (FALCONER).

Bibliography

Anandan, J. 1992, Nature, 360, 307
Bazargan, K. 1992, in Intl Symp on Display Holography, Vol. 1600, International Society for Optics and Photonics, 178–182
Berry, M. V. 1984, Proc. R. Soc. Lond. A, 392, 45
Bjelkhagen, H. I., & Mirlis, E. 2008, Applied optics, 47, A123
Brown, B., & Lohmann, A. 1969, IBM Journal of research and Development, 13, 160
Brown, B. R., & Lohmann, A. W. 1966, Applied Optics, 5, 967
Chang, C., Xia, J., Yang, L., et al. 2015, Applied optics, 54, 6994
Chigrinov, V. G., Kozenkov, V. M., & Kwok, H.-S. 2008, Photoalignment of liquid crystalline materials: physics and applications, Vol. 17 (John Wiley & Sons)
De Sio, L., Roberts, D. E., Liao, Z., et al. 2016, Optics express, 24, 18297
Doelman, D. S., Snik, F., Warriner, N. Z., & Escuti, M. J. 2017, in Techniques and Instrumentation for Detection of Exoplanets VIII, Vol. 10400, International Society for Optics and Photonics, 104000U
Escuti, M. J., Kim, J., & Kudenov, M. W. 2016, Optics and Photonics News, 27, 22
Gerchberg, R. W., & Saxton, W. O. 1972, Optik, 35, 237

Glückstad, J. 1996, Optics Communications, 130, 225
Grier, D. G. 2012, Multi-color holographic optical trapping, Google Patents
Hasman, E., Kleiner, V., Biener, G., & Niv, A. 2003, Applied physics letters, 82, 328
Hayasaki, Y., Itoh, M., Yatagai, T., & Nishida, N. 1999, Optical review, 6, 24
Huang, K., Dong, Z., Mei, S., et al. 2016, Laser & Photonics Reviews, 10, 500
Huang, L., Chen, X., Mühlenbernd, H., et al. 2013, Nature communications, 4, 2808
Ito, T., & Okano, K. 2004, Optics Express, 12, 4320
Jesacher, A., Bernet, S., & Ritsch-Marte, M. 2014, Optics express, 22, 20530
Kim, J., Li, Y., Miskiewicz, M. N., et al. 2015, Optica, 2, 958
Komanduri, R. K., Lawler, K. F., & Escuti, M. J. 2013, Optics Express, 21, 404
Kowalczyk, A. P., Makowski, M., Ducin, I., Sypek, M., & Kolodziejczyk, A. 2018, Optics Express, 26, 17158
Kuratomi, Y., Sekiya, K., Satoh, H., et al. 2010, JOSA A, 27, 1812
Leith, E., Kozma, A., Upatnieks, J., Marks, J., & Massey, N. 1966, Applied optics, 5, 1303
Lohmann, A. W. 2008, Optics and Photonics News, 19, 36
Lyot, B. 1939, Monthly Notices of the Royal Astronomical Society, 99, 580
Makowski, M., Sypek, M., & Kolodziejczyk, A. 2008, Optics express, 16, 11618
Miskiewicz, M. N., & Escuti, M. J. 2014, Optics Express, 22, 12691
Mueller, J. B., Rubin, N. A., Devlin, R. C., Groever, B., & Capasso, F. 2017, Physical review letters, 118, 113901
Ni, X., Kildishev, A. V., & Shalaev, V. M. 2013, Nature communications, 4, 2807
Oh, C., & Escuti, M. J. 2008, Optics letters, 33, 2287
Otten, G. P., Snik, F., Kenworthy, M. A., et al. 2014, in Advances in Optical and Mechanical Technologies for Telescopes and Instrumentation, Vol. 9151, International Society for Optics and Photonics, 91511R
Otten, G. P., Snik, F., Kenworthy, M. A., et al. 2017, The Astrophysical Journal, 834, 175
Palima, D., & Glückstad, J. 2008, Optics express, 16, 1331
Pan, J.-W., & Shih, C.-H. 2014, Optics express, 22, 6464
Pancharatnam, S. 1955in , Springer, 137–144
Peercy, M. S., & Hesselink, L. 1994, Applied optics, 33, 6811
Por, E. H., Haffert, S. Y., Radhakrishnan, V. M., et al. 2018, in Proc. SPIE, Vol. 10703, Adaptive Optics Systems VI
Shimobaba, T., & Ito, T. 2003, Optical review, 10, 339
Shiraki, A., Takada, N., Niwa, M., et al. 2009, Optics express, 17, 16038
Slinger, C., Cameron, C., & Stanley, M. 2005, Computer, 38, 46
Snik, F., Otten, G., Kenworthy, M., et al. 2012, in Modern Technologies in Space-and Ground-based Telescopes and Instrumentation II, Vol. 8450, International Society for Optics and Photonics, 84500M
Tsuchiyama, Y., & Matsushima, K. 2017, Optics express, 25, 2016
Xiang, X., Kim, J., & Escuti, M. J. 2017a, Crystals, 7, 383
—. 2018, Scientific Reports, 8, 7202
Xiang, X., Kim, J., Komanduri, R., & Escuti, M. J. 2017b, Optics Express, 25, 19298
Yaraş, F., Kang, H., & Onural, L. 2010, Journal of display technology, 6, 443